In vitro and *in vivo* characterization of several functionalized ultrasmall particles of iron oxide, vectorized against amyloid plaques and potentially able to cross the blood–brain barrier: toward earlier diagnosis of Alzheimer's disease by molecular imaging

Emilie Ansciaux[a], Carmen Burtea[a], Sophie Laurent[a], Deborah Crombez[a], Denis Nonclercq[b], Luce Vander Elst[a] and Robert N. Muller[a,c]*

Alzheimer's disease (AD) is a neurodegenerative disorder most often diagnosed 10 years after its onset and development. It is characterized by the accumulation of amyloid-β peptide (ABP) into amyloid plaques between nerve cells, which produces a massive local neurodegeneration. Molecular magnetic resonance imaging allows diagnosis of AD by showing ABP accumulation in the brain. The ultrasmall particles of iron oxide (USPIO) derivatives proposed in the present work were functionalized with peptides that present an affinity for ABP, independently of its state of aggregation. Their nanomolar K_d* confirms the high affinity of our vectorized contrast agents (VCA) for ABP and therefore their high labeling potential, specificity and sensitivity. Their lack of toxicity has been demonstrated, both by *in vitro* studies using the MTT method on several cell types, and by *in vivo* investigations with assessment of renal and hepatic biomarkers and by histopathology evaluation. The results of biodistribution studies corroborated by MRI demonstrate that USPIO-PHO (USPIO coupled to peptide C-IPLPFYN-C) are able to cross the blood–brain barrier without any facilitating strategy, and accumulates in the brain 90 min after its injection in NMRI mice. None of the USPIO derivatives were found in any organs one week after administration. To conclude, USPIO-PHO seems to have a genuine potential for labeling amyloid plaques in the brain; it has a nanomolar binding affinity, no toxic effects, and its elimination half-life is about 3 h. Further tests will be made on transgenic mice, aimed at confirming the potential of early AD diagnosis using our VCA. Copyright © 2014 John Wiley & Sons, Ltd.

Additional supporting information may be found in the online version of this article at the publisher's web site.

Keywords: Alzheimer's disease; MRI; functionalized iron oxide nanoparticles; amyloid-β peptide; contrast agents; blood–brain barrier

1. INTRODUCTION

Alzheimer's disease (AD) is a neurodegenerative disorder whose main symptom is a progressive and irreversible loss of cognitive abilities, including those related to memory, reflection, language and mood, with three nonspecific phases in which symptoms are intertwined. Nonetheless, in most cases the presumptive diagnosis is made almost 10 years after onset and development of the disease, when the brain is already severely damaged. Among these phases, mild cognitive impairment (MCI) defines a higher level of deficit than expected for a specific age and socio-cultural subject, although not severe enough to be considered as a dementia (1,2).

Several hypotheses have been proposed with regard to the fundamental molecular mechanism leading to neuronal loss: amyloid (3), tau (4), oxidative stress (5), soluble oligomers (6), inflammatory pathway (7) and loss of cholinergic neurons (8). Nevertheless, currently no hypothesis has as yet been clearly validated. Accumulation of amyloid-β peptide (ABP) and neurofibrillary tangles leads

to synaptic function impairment, ultimately producing massive local neurodegeneration. ABP is derived from cleavage of a precursor protein, named amyloid-precursor protein (APP), and

*   Correspondence to: R. N. Muller, Center for Microscopy and Molecular Imaging, 8, rue Adrienne Bolland, 6041, Gosselies, Belgium. E-mail: robert.muller@umons.ac.be

a   E. Ansciaux, C. Burtea, S. Laurent, D. Crombez, L. Vander Elst, R. N. Muller
Department of General, Organic and Biomedical Chemistry, NMR and Molecular Imaging Laboratory, University of Mons, Avenue Maistriau 19, Mendeleev Building, B-7000, Mons, Belgium

b   D. Nonclercq
Laboratory of Histology, University of Mons, Pentagon – 1B, 6 Avenue du Champ de Mars, B-7000, Mons, Belgium

c   R. N. Muller
Center for Microscopy and Molecular Imaging, 8, rue Adrienne Bolland, 6041, Gosselies, Belgium

can self-aggregate into very toxic amyloid-β oligomers and then into toxic amyloid fibres, which are the hallmark of AD pathogenesis (9–12). The blood–brain barrier (BBB) does not normally allow simple diffusion of ABP from the blood to the brain and regulates the brain concentration of ABP (11,13). With aging, the BBB undergoes alterations and expression of transporters varies. The efflux transporters (from brain to blood) decrease, while the influx carriers (from brain to blood) increase (14,15), which causes an increase in amyloid deposits in the brain (16,17).

Among potential plasma or cerebrospinal fluid biomarkers, ABP and tau are at the center of attention because it is suspected that their overproduction and biochemical changes precede the clinical symptoms by decades (18). Unfortunately, lumbar puncture is invasive and is unlikely to become a routine procedure for AD diagnosis in clinical geriatrics, whereas plasma levels of tau and of ABP are too low to be analyzed. In addition, a change in blood concentration does not necessarily reflect a change in the brain (19). Faced with these problems, molecular imaging becomes a more practical alternative, enabling *in vivo* characterization and measurement of biological processes at the cellular and molecular levels, ideally reflecting the early molecular abnormalities of diseases, as opposed to conventional imaging techniques that only show the morphological effects of these alterations (20,21). However, molecular imaging requires the development of safe, specific imaging tracers targeted to a distinct pathological biomarker, allowing its visualization with high sensitivity and thus ensuring an accurate and reliable diagnosis of the concerned pathology. In the case of AD, nuclear tracers based on analogs of Congo Red, Thioflavin-T and stilbene are already available, but only Amyvid^{TM} [Florbetapir F18, (*E*)-2-{2-[2-(2-[^{18}F] Fluoroethoxy)ethoxy]ethoxy}-5-(4-   methylaminostyryl)pyridine, a derivative of stilbene] has been approved for clinical practice, in 2012 (22–24).

Despite their excellent sensitivity, these compounds are not specific to AD pathology, but to any amyloidosis condition, while nuclear medicine technology has an anatomical resolution in the range of millimeters and is not compatible with recurrent monitoring of AD patients. Owing to its submillimetric anatomical resolution and its typical noninvasiveness enabling iterative patient monitoring, magnetic resonance imaging (MRI) seems to be an optimal alternative to nuclear imaging technologies. The molecular imaging probes proposed so far for MRI applications were functionalized with peptides derived from ABP (25–27) that are themselves potentially toxic by virtue of their ability to promote ABP aggregation. It also appears that the iron content in the amyloid plaques allows their detection with specific MRI sequences without the need for using contrast agents (28). Unfortunately, this requires very high fields (greater than 7 T) and very long acquisition times (several hours), which are not achievable in clinical practice. In addition, the detection of endogenous iron depends on the nature of the amyloid plaques (not all amyloid plaques contain iron) and the stage of the disease, with larger plaques containing higher amounts of iron, allowing easier detection (11).

The phage display technique is suitable for finding small original probes that can be used to vectorize contrast agents for MRI detection of amyloid plaques. Pursuing this goal, a randomized phage display library of cyclic heptapeptides was previously screened by our group on ABP$_{1–42}$ (11). Two peptides stood out by virtue of their good ABP affinity, PHO (C-IPLPFYN-C) and PHI (C-FRHMTEQ-C), respectively. A third peptide (LIAIMA, encoded as P1), derived from a linear peptide library designed

from the amino acid sequence of ABP$_{1–42}$, was developed during our previous studies by soft oligonucleotide-directed mutagenesis (29). The three peptides were able to stain the outskirts of senile plaques or all of the diffuse amyloid plaques on brain sections of APP/PS1 DE9 transgenic mice. For MRI evaluation, these peptides were coupled to carboxyl groups exposed by the coating of ultrasmall particles of iron oxide (USPIO), which were also coated with polyethylene glycol (PEG) to enhance their stealthiness. Some of these contrast agents have also been coupled with putrescine (put), with the aim of improving their ability to cross the BBB. Five functionalized contrast agents were thus obtained, USPIO-PHO, USPIO-PHI, USPIO-P1, USPIO-PHO-put and USPIO-PHI-put. USPIO coated with PEG alone and USPIO-PEG coupled only with put (USPIO-put) were used as controls. They were characterized in the present work by a battery of *in vitro* and *in vivo* screening methods (affinity for ABP, cytotoxicity, endocytosis, biodistribution, pharmacokinetics and BBB crossing) (30,31), aiming to develop a vectorized contrast agent able to diagnose AD early, and to assess future therapeutic strategies using MRI.

2. RESULTS

2.1.   Apparent dissociation constant K_d* for ABP$_{1–42}$ binding

The K_d* values of our vectorized contrast agents for ABP$_{1–42}$ binding are summarized in Table 1. They show 20-fold higher affinities for the vectorized contrast agents coupled to both peptide and putrescine than those coupled with peptide alone. Regardless of this difference with or without coupling to putrescine, our vectorized contrast agents show K_d* values in the nanomolar range, indicating a high affinity for ABP$_{1–42}$ and the retention of the peptides' affinity after grafting to nanoparticles. The specific binding to ABP$_{1–42}$ is proven by the negligible interaction with BSA (Fig. S1 in the Supporting Information) and the absence of any ABP$_{1–42}$ affinity of the negative control contrast agents, USPIO-PEG and USPIO-put, respectively.

2.2.   *In vitro* cytotoxic effect on cellular cultures assessed by MTT assay

The MTT [3-(4,5-dimethylthiazol-2-yl)-2,5-diphenyl tetrazolium bromide] method was used to evaluate the viability of N18TG2 neurons, HUVEC and HepaRG hepatocytes after incubation with contrast agents at an iron concentration of 2 mM for 2 and 24 h (Fig. 1). Cells not incubated with contrast agents were used as negative controls. No significant cytotoxic effect was observed, the cell viability never falling below 94%.

Table 1. Evaluation of the apparent dissociation constants of the vectorized contrast agents for β-amyloid$_{1–42}$

Vectorized contrast agents	Mean K_d* ± SEM (nM)
USPIO-PHO	30.3 ± 1.15**
USPIO-PHI	33.4 ± 3.75**
USPIO-P1	53.8 ± 2.95
USPIO-PHO-put	1.58 ± 1.06
USPIO-PHI-put	1.45 ± 0.11

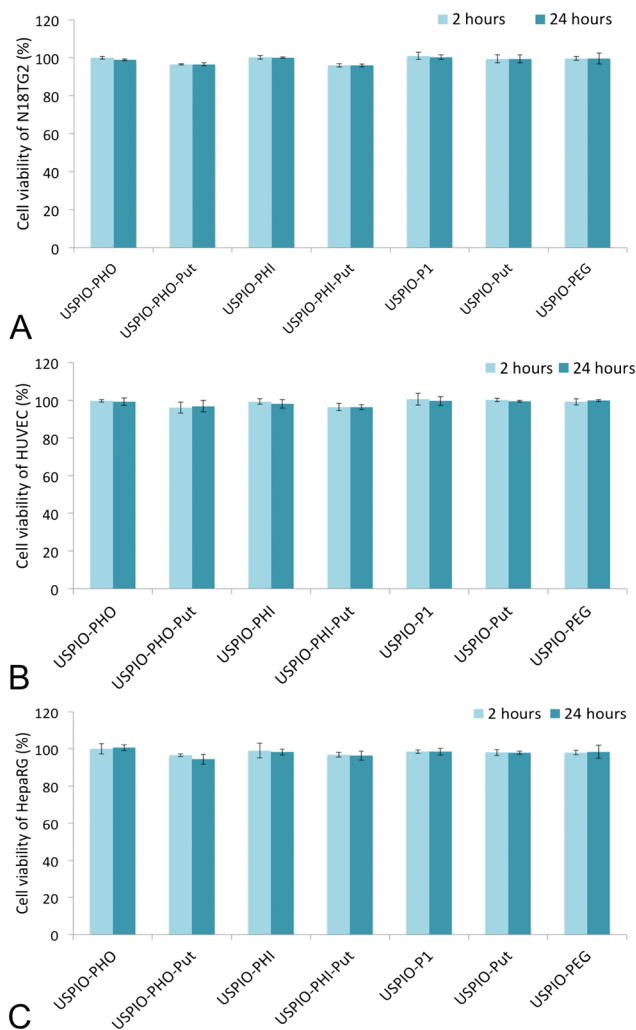** = $p < 0.01$ compared with USPIO-P(x)-put.

Figure 1. Histogram showing the cell viability of N18TG2 neurons (A), endothelial cells (B) and HepaRG hepatocytes (C) after 2 or 24 h of incubation with USPIO derivatives at an iron concentration of 2 mM.

2.3. Evaluation of cellular internalization of USPIO derivatives via *in vitro* assessment of cellular lysosomes by fluorescent labeling and measurement of iron concentration

The quantity of lysosomes in the cells indirectly demonstrates the rate of the contrast agents' endocytosis. The results reflect higher lysosome content of the N18TG2 neurons (Fig. 2a) and HUVEC (Fig. 3a) incubated with USPIO-PHO, which is corroborated by the semi-quantitative analysis shown in Figs. 2(b/c) and 3(b/c). The statistical analysis (Tables 2 and 3) indicates a significant difference ($p < 0.01$) between these cells and either controls, USPIO-put (for N18TG2 neurons) or USPIO-PEG (for HUVEC). With the exception of USPIO-P1 in HUVEC, the lysosome content was higher in each case compared with negative controls, which may indicate endocytosis of our contrast agents. When compared with USPIO-PEG, USPIO-PHO induced significantly higher lysosome content in HUVEC ($p < 0.01$), but not in N18TG2 neurons ($p > 0.05$). The comparison with USPIO-put in N18TG2 neurons reflects significantly higher lysosome content for the cells incubated with USPIO-PHO ($p < 0.01$), USPIO-P1 ($p < 0.01$) and USPIO-PHO-put ($p < 0.05$).

The results of this study have shown that putrescine does not improve the uptake of USPIO derivatives by cells, either when coupled alone or in association with PHO or PHI peptides. The N18TG2 neurons incubated in the same conditions as for the lysosome labeling were analyzed by optical microscopy (Fig. S2 in the Supporting Information), which have clearly shown that USPIO-PHO-put and USPIO-PHI-put aggregated in culture conditions. This could explain the low level of endocytosis observed by fluorescent labeling of lysosomes. Aiming to confirm the effect of physiological media on USPIO agglomeration, we measured their hydrodynamic size by photon correlation spectroscopy (PCS) after incubating them in various buffers and culture media (Table S1 in the Supporting Information). These results confirmed our observations obtained by optical microscopy.

The uptake of USPIO-PHO by N18TG2 neurons and HUVEC was then confirmed by the measurement of iron concentration in cell samples after incubation in the same conditions as for lysosome labeling (Fig. S3 in the Supporting Information). Significantly higher iron concentration ($p < 0.01$) was found in HUVEC incubated with USPIO-PHO as compared with USPIO-PEG. Although N18TG2 neurons have taken more USPIO-PHO than USPIO-PEG, the difference between these contrast agents was not significant.

2.4. *In vivo* evaluation of the pharmacokinetics and biodistribution

The pharmacokinetic parameters ($T_{e1/2}$, Cl_{tot} and VD_{ss}) were determined for the following contrast agents: USPIO-PHO, USPIO-PHI, USPIO-P1 and USPIO-PEG, used as a control. The results in Table 4 show that USPIO-P1 and USPIO-PEG have equivalent elimination half-lives ($T_{e1/2}$), which are also the longest (about 4 h 30 min) among the investigated USPIO derivatives. The $T_{e1/2}$ of USPIO-PHO is shorter (about 3 h), whereas USPIO-PHI is characterized by the fastest elimination ($T_{e1/2}$ of 1 h 15 min).

Biodistribution was evaluated by relaxometry on organs of NMRI mice, collected at specific times after intravenous injection of our contrast agents, by treating the T_2 relaxation curves with a bi-exponential equation. This provided two components of the water proton relaxation rate, fast (R_{2-1}, Fig. 4) and slow (R_{2-2}, Fig. S4 in the Supporting Information), respectively. The fractions of one or the other components of the T_2 relaxation curves ranged from 25% to more than 50%. The results suggest that USPIO-PHO could be able to cross the BBB 90 min after intravenous injection, considering the 313% increase in R_{2-1} as compared with the negative control. Surprisingly, the R_{2-1} effect produced by USPIO-PHO coupled to putrescine (USPIO-PHO-put) is decreased compared with USPIO-PHO (149% compared with negative control, 90 min after administration), suggesting a lower level of brain penetration. Contrast agents vectorized with the PHI peptide either coupled (USPIO-PHI-put) or not (USPIO-PHI) to putrescine do not seem to penetrate the brain, the same as USPIO-put. These results demonstrate that putrescine does not facilitate crossing the BBB in the case of this class of nanoparticles. USPIO-P1 has a certain ability to target the brain, but this is lower and delayed as compared with USPIO-PHO (198% compared with negative control, 150 min after administration). Excepting the PHI derivatives and USPIO-put, the vectorized contrast agents were generally captured by the liver 2 h 30 min after administration, although the capture of USPIO-PHO was slower, allowing it to accumulate in the brain. At more advanced times (i.e. starting one week after administration),
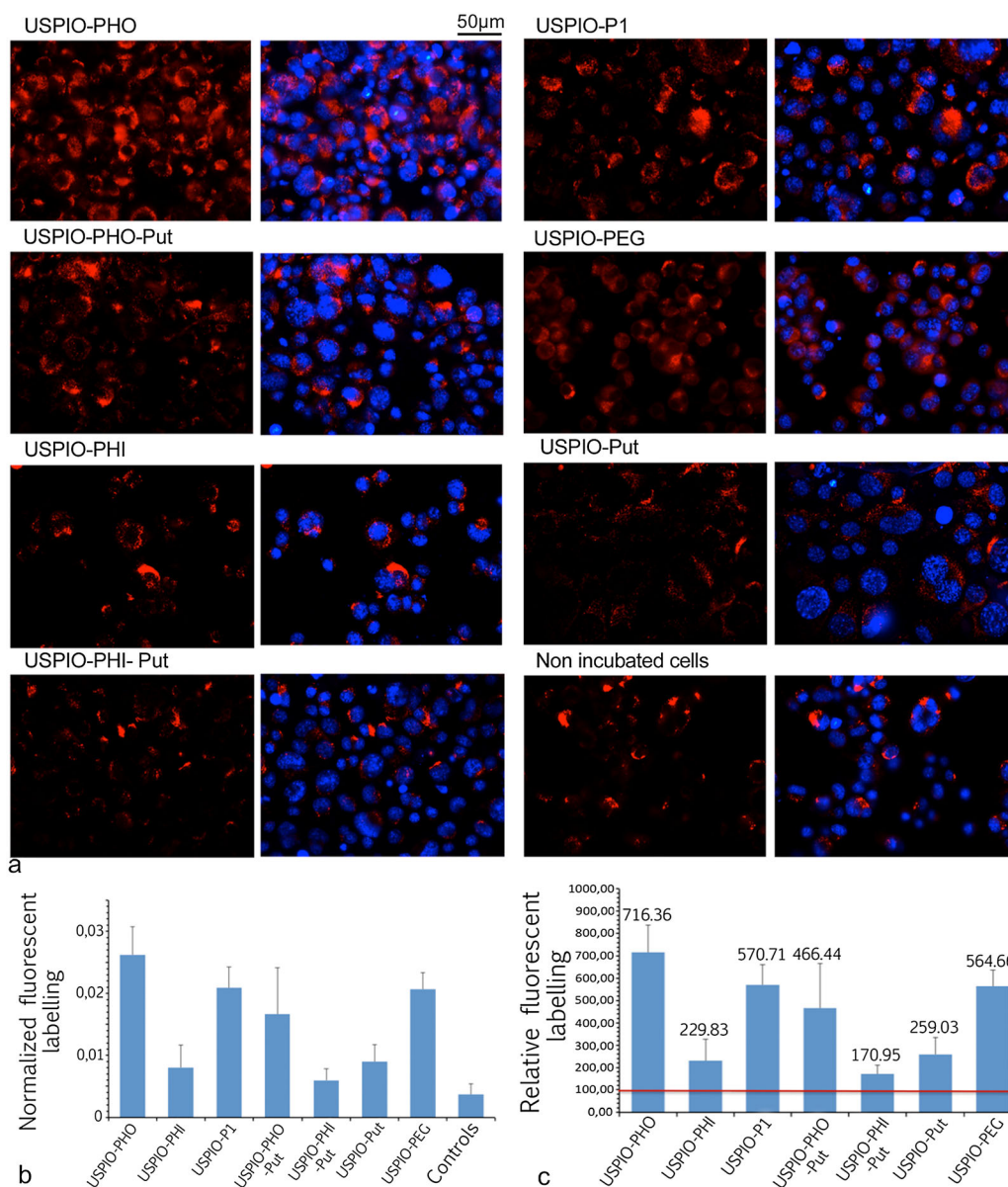
Figure 2. Fluorescent lysosome labeling in N18TG2 neurons incubated for 2 h with various USPIO derivatives at an iron concentration of 2 mM. (a) Microphotographs of N18TG2 neurons showing, by fluorescence microscopy, the lysosomes (left) and the merged pictures of lysosomes and nuclei (right). (b, c) Histograms showing the normalized fluorescent labeling (b) and the relative fluorescent labeling (c) of the lysosomes (percentage calculated from values obtained for cells incubated with culture medium alone) in N18TG2 neurons.

none of the contrast agents were found either in the brain or in the liver.

The results obtained on kidneys suggest that USPIO derivatives tend to accumulate gradually in this organ as their plasma concentration decreases. The urine concentration of our vectorized contrast agents (USPIO-PHO, USPIO-PHI and UPIO-P1) was compared with that of USPIO-PEG; with the exception of USPIO-PHI, all the other contrast agents attained a urinary peak 12 h after administration, which attests to their partial renal excretion. Among them, USPIO-PHO is notable for having the highest urinary concentration. The results obtained in the spleen and lungs suggest that our USPIO derivatives are just passing through these organs, since their effect attains a peak at 90 min after administration, followed by a drop 1 h later.

2.5. Evaluation of *in vivo* toxicity by measuring plasma alanine transaminase activity and creatinine concentration in urine samples

To assess the toxicity induced by our vectorized contrast agents *in vivo*, the enzymatic activity of alanine transaminase (ALT) was evaluated in blood samples collected during the *in vivo* pharmacokinetic experiments. This enzyme is highly expressed in the liver and its increased activity in blood plasma is a sign of hepatic cytolysis, a progressive destruction of liver cells. In addition, the creatinine concentration was evaluated in urine samples taken during the same pharmacokinetic studies. As a breakdown product of creatinine phosphate in muscle, creatinine is entirely eliminated by the kidneys in urine, thus being a good indicator of renal function.
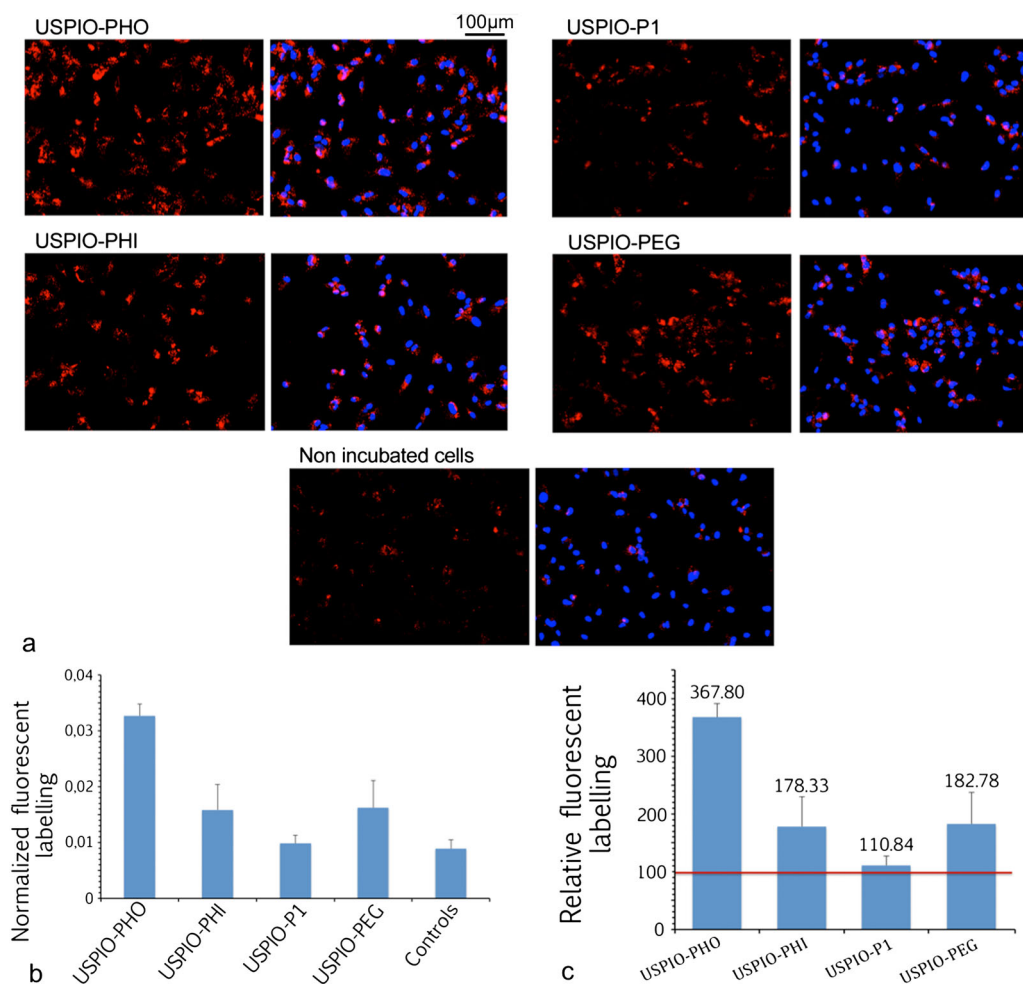
Figure 3. Fluorescent lysosome labeling in HUVEC incubated for 2 h with various USPIO derivatives at an iron concentration of 2 mM. (a) Microphotographs of HUVEC showing, by fluorescence microscopy, the lysosomes (left) and the merged pictures of lysosomes and nuclei (right). (b, c) Histograms showing the normalized fluorescent labeling (b) and relative fluorescent labeling (c) of the lysosomes (percentage calculated from values obtained for cells incubated with culture medium alone) in HUVEC.

The enzymatic activity of ALT in blood plasma (Fig. 5) was equivalent to controls (not injected mice) in all experimental groups for all post-injection times considered. A significant increase ($p < 0.01$) in urine creatinine concentration was observed 12 h after USPIO-PHO administration, but its level returned to normal within 24 h after injection. All the other experimental groups presented a significant decrease in urinary creatinine during the first hours after administration (4 h maximum), but this returned to normal immediately after that.

2.6. Evaluation of the integrity of the sampled organs by Masson's Trichrome staining

Organs (heart, lung, spleen, liver, kidney and brain) from NMRI mice injected with USPIO derivatives and from controls (uninjected NMRI mice) were analyzed after Masson's trichrome staining to evaluate the tissue integrity. Figure 6 shows microphotographs of histological sections taken from controls and from mice injected with USPIO-PHO and sacrificed 1 week later. Sections obtained from mice injected with all the other vectorized contrast agents were morphologically similar. The results show a lack of tissue or cellular damage to any of the harvested organs.

2.7. In vivo MRI evaluation of USPIO-PHO's ability to cross the BBB

Based on the results presented above, USPIO-PHO was selected for in vivo MRI studies and USPIO-PEG was used as a negative control. Several MRI sequences (i.e. T_2-weighted spin echo, as well as T_2*-weighted 2D and 3D gradient echo MRI sequences) were assessed on NMRI mice with the intent of developing a protocol able to reveal the aptitude of USPIO-PHO to cross the BBB. Representative images are assembled in Fig. 7, where the rostral midbrain is shown in the area proximal to the lateral and third ventricles. All of the MRI sequences revealed that USPIO-PHO produces a negative contrast in this area of the brain, which may be related to its ability to cross the BBB.

The percentage distribution of black pixels in the cortex and subcortical areas of the brain are represented as mesh plots in Fig. 8, where their evolution over time is expressed as a percentage as compared with pre-contrast images. The results confirm that USPIO-PHO indeed produced a negative contrast in subcortical areas of the brain, probably related to its diffusion through the blood–cerebrospinal fluid barrier (BCSFB) of the choroid plexus. The negative contrast produced by USPIO-PEG was also evident in the cortical areas, which may be related to its circulation in the blood stream of the major blood vessels of the brain.

Table 2. Statistical analysis of the lysosome labeling in N18TG2 neurons incubated with various contrast agents

	p-Value	95% confidence interval for difference of means
Control vs		
USPIO-PHO	<0.01	−0.0275 to −0.0176
USPIO-PHI	<0.05	−0.0082 to −0.0006
USPIO-P1	<0.01	−0.0212 to −0.0133
USPIO-PHO-put	<0.01	−0.0205 to −0.0055
USPIO-PHI-put	<0.05	−0.0045 to −0.0001
USPIO-put	<0.01	−0.0084 to −0.0023
USPIO-PEG	<0.01	−0.0210 to −0.0131
USPIO-PEG vs		
USPIO-PHO	>0.05	−0.0136 to 0.0025
USPIO-PHI	<0.01	0.00689 to 0.0184
USPIO-P1	>0.05	−0.0066 to 0.0062
USPIO-PHO-put	>0.05	−0.0074 to 0.0155
USPIO-PHI-put	<0.01	0.0113 to 0.0181
USPIO-put	<0.01	0.0071 to 0.0163
USPIO-put vs		
USPIO-PHO	<0.01	−0.0220 to −0.0125
USPIO-PHI	>0.05	−0.0027 to 0.0047
USPIO-P1	<0.01	−0.0160 to −0.0078
USPIO-PHO-put	<0.05	−0.0143 to −0.0010
USPIO-PHI-put	<0.05	0.0005 to 0.0056
USPIO-put	<0.01	−0.0163 to −0.0071
USPIO-P(x)-put vs		
USPIO-PHO	<0.05	0.0004 to 0.0188
USPIO-PHI	>0.05	−0.0011 to 0.0052

Table 3. Statistical analysis of the lysosome labeling in HUVEC incubated with various contrast agents

	p-Value	95% confidence interval for difference of means
Control vs		
USPIO-PHO	<0.01	−0.0261 to −0.0215
USPIO-PHI	<0.01	−0.0113 to −0.0027
USPIO-P1	>0.05	−0.0029 to 0.0010
USPIO-PEG	<0.01	−0.0118 to −0.0030
USPIO-PEG vs		
USPIO-PHO	<0.01	−0.0210 to −0.0119
USPIO-PHI	>0.05	−0.0051 to 0.0059
USPIO-P1	<0.01	0.0020 to 0.0108

Table 4. Pharmacokinetic parameters obtained in NMRI mice

Vectorized contrast agents	$T_{e1/2}$ (min)	V_{Dss} (l/kg)	Cl_{tot} (ml/min/kg)
USPIO-PHO	184	0.0516	0.194
USPIO-PHI	75	0.0565	0.524
USPIO-P1	276	0.0473	0.119
USPIO-PEG	284	0.0475	0.116

2.8. Validation of USPIO-PHO's ability to cross the BBB by histochemistry

The brains of mice injected with either USPIO-PHO or USPIO-PEG were sampled 90 min after administration and the presence of USPIO derivatives inside the brain parenchyma was confirmed by Perls'-DAB staining. Figure 9 corroborates the MRI data by revealing the presence of USPIO-PHO nanoparticles inside the brain, where they are homogenously distributed, but are more concentrated in the choroid plexus, around the ventricles (the dorsal third ventricle in Fig. 9), beneath the hippocampus and in the cortical area above the third ventricle. Interestingly, USPIO-PEG is also present in similar areas of the brain, but at a much lower level.

3. DISCUSSIONS AND CONCLUSIONS

Among the different phases of AD, MCI is of great importance because it can predict patients having a major risk of subsequently developing dementia (1,17). The correct diagnosis of MCI patients would enable prevention of AD or delay its progression if a treatment is initiated in earlier stages of the disease (32–35). Therefore, there is an increasing demand to develop reliable diagnostic tools able to detect ABP even before the appearance of amyloid plaques, at the very first stages of MCI.

The USPIO derivatives proposed in the present work were functionalized with peptides that present an affinity for ABP, independently of its state of aggregation. USPIO belongs to a new class of MRI contrast agents that are particularly interesting for molecular imaging owing to their excellent MRI efficacy, biocompatibility, and biodegradability. The blood half-life of this material is significantly prolonged by coating it with hydrophilic polymers, such as PEG, which reduces its opsonisation and clearance by the reticuloendothelial system, thus improving the targeting of specific biomarkers. The nanomolar K_d^* confirms the high affinities of our vectorized contrast agents for ABP and therefore their high labeling potential, specificity and sensitivity. Moreover, the specific interaction of peptides PHO and PHI with ABP was previously confirmed by the absence of any affinity for amylin, another amyloidogenic peptide that is involved in type 2 diabetes (12). Putrescine apparently improves the K_d^* by a factor of 20, but this unusual behavior of contrast agents functionalized with both peptide and putrescine is explainable by their tendency to agglomerate in culture media and incubation buffers used in experimentation. Many studies have already proven that some iron oxide nanoparticles may interact with serum proteins or other factors in the culture media (36). This interaction leads to a ring of proteins, named protein corona, which surrounds iron oxide nanoparticles and causes their aggregation, modifying their ability to interact with biological systems.

Among the investigated contrast agents, USPIO-PHO was preferentially endocytosed by both N18TG2 neurons and HUVEC. The experimental data obtained to date do not allow us to conclude with regard to its mechanism of endocytosis, although the hydrophobic properties of PHO peptide may favor its attachment to the cell membranes, pulling down the nanoparticles inside the endocytic pits. The endocytosis of USPIO-PHO could facilitate the BBB crossing over, followed by their eventual capture inside the neurons. If this late event will be confirmed by *in vivo* data, the detection of intracellular Aβ oligomers would render them advantageous for the early diagnosis of AD. Indeed, recent experimental data suggest that prefibrillar soluble Aβ
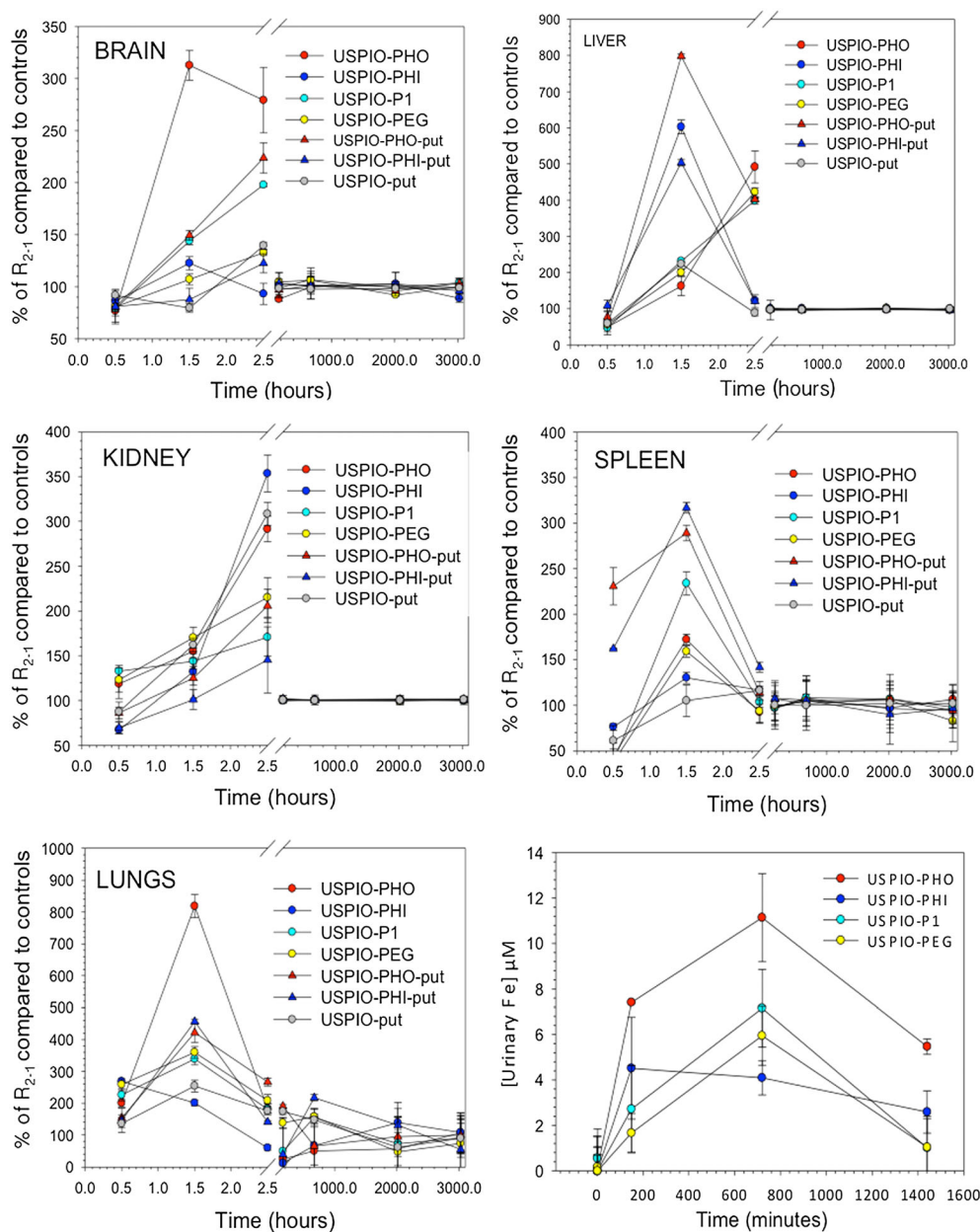
Figure 4. Graphs showing the biodistribution of USPIO derivatives expressed as a percentage of R_{2-1} (the fast component of R_2) compared with negative controls (i.e. not injected with contrast agents). The urine concentration is also shown for some of the contrast agents.

oligomers accumulate in the intracellular space and induce the AD-related synaptic dysfunction and severe cognitive impairment, being more cytotoxic than the insoluble fibrillar aggregates found in extracellular plaques (37,38).

An absence of toxicity was demonstrated for all our USPIO derivatives, both by *in vitro* studies using the MTT method on several cell types, and by *in vivo* investigations with assessment of renal and hepatic biomarkers and histopathology evaluation. Variations in urinary creatinine concentrations were observed during the first hours after administration (i.e. maximum 12 h), but they returned to normal within 24 h. This could be explained by a dilution of creatinine in a large volume of urine or by a temporary disruption of its excretion. In the case of USPIO-PHO, the creatinine concentration was increased 12 h after injection, probably owing to a decrease in urine volume or by an osmotic effect caused by USPIO-PHO itself, present at a high level in the urine

instead of being eliminated by macrophages. According to the literature, the diameter of USPIO is greater than that of fenestrated capillaries in the kidney, thereby preventing their excretion. However, the diameter of these capillaries can reach about a 100 nm (39), theoretically allowing our vectorized contrast agents to cross them. According to another hypothesis, podocytes may prevent nanoparticles from passing into the Bowman's space and finally arriving in the urine. Intraglomerular mesangial cells could also make a contribution to the clearance of nanoparticles owing to their phagocytic properties. Whatever the mechanism of nanoparticle restriction from urinary clearance, our results confirmed their ability to cross over the renal filter, especially in the case of USPIO-PHO.

Biodistribution studies have shown the inefficiency of putrescine to facilitate the USPIOs crossing the BBB. Although previous studies demonstrated the ability of polyamines to increase the
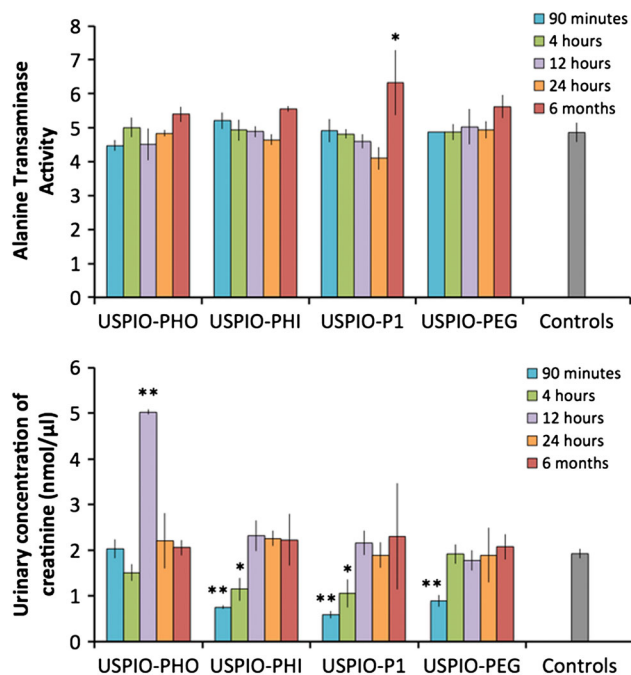
Figure 5. Evaluation of *in vivo* toxicity by measuring plasma alanine transaminase (top) and creatinine concentrations in urine samples (bottom). * $p < 0.05$, ** $p < 0.01$ compared with controls.

permeability at the BBB of proteins (40) and of amyloid plaque-targeted imaging probes (26,41), this pharmacological strategy does not seem to be useful for the brain delivery of nanoparticulate contrast media such as USPIO, which is driven by an endocytic pathway instead of a membrane transporter mechanism. The agglomeration of USPIO derivatives functionalized with both putrescine and peptides would have furthermore hampered their brain penetration via a transcytosis mechanism, which is restricted to submicrometric nanoparticulate material. For further studies, it will be interesting to assess other strategies to improve the brain access of our contrast agents, such as the use of specific molecules like Cereport (RMP-7, labradimil, lobradimil) (42–44) or mannitol (10).

The results of the biodistribution study were corroborated by the MRI and histochemistry studies, demonstrating that USPIO-PHO could cross the BBB without any facilitating strategy and accumulate in the brain 90 min after its injection in NMRI mice. USPIO-PHO is characterized by a slow blood clearance, but this is ~35% faster than that of USPIO-PEG and ~33% faster than that of USPIO-P1. The prolonged elimination half-life of USPIO-PEG and of USPIO-P1 did not produce a comparable T_2 or T_2^* effect on brain as that of USPIO-PHO, as shown by relaxometry or by MRI at early time points, that is, before 120 min. This effect cannot be explained either by the r_2 value, which is similar in blood plasma for all these USPIO derivatives. As explained above, the hydrophobic properties of USPIO-PHO [log$D_{7.4}$ of 2.5 for peptide PHO (29)] may have enabled its binding to the cell membranes followed by endocytosis, although a permissive effect of a peptide transporter (45,46) could not be neglected. For instance, TAPL (Q9NP78) is a multi-pass membrane protein located in lysosome membrane and probably in membrane rafts, which has moderate expression levels in brain and spinal cord and displays broad peptide length specificity, favoring positively charged, aromatic or hydrophobic residues in the N- and C-terminal positions. Such peptide transporter could have contributed to the brain delivery of USPIO-PHO, which is exclusively composed of hydrophobic residues. Although this delivery is not very large, some diffusion of USPIO-PHO within the brain parenchyma seems to be probable. The results of the histochemistry study suggest that nanoparticles diffuse into the brain via the BCSFB, which is composed of the fenestrated choroidal vessels and the ependymal cells that present tight junctions and form an interface between the blood and CSF. The tight junctions of BCSFB are 'leakier' owing to the particular claudins expressed at this level, whereas the endocytotic activity is stronger at this level owing to intense metabolic activity and synthetic functions of the choroid plexus (47).

With regard to the later time points of the biodistribution study, none of the USPIO derivatives were found in any organs one week after administration, which is advantageous from the viewpoint of their eventual toxicological outcome.

Nanomedicine has recently proposed a broad range of nanoparticulate scaffolds with tuneable chemical surfaces, potentially able to enhance the drug transport across the BBB. The physicochemical and biomimetic properties of the nanoparticle's surface (e.g. positive charges, protein corona) seem to drive this phenomenon, and the BBB passage without functionalization or by adsorptive-mediated transcytosis has already been described. Gold and silica nanoparticles were shown to reach the brain and accumulate in neurons by a mechanism that has not yet been explained and in the absence of any molecular functionalization (48).

PEG is generally used as a stealthy coating material that limits the formation of protein corona and the uptake of nanoparticles by the reticuloendothelial system, but it is also able to facilitate the nanoparticles' diffusion within brain parenchyma. Using PEG-coated nanoparticles, it was estimated that extracellular space of the brain parenchyma is crossed by pores of at least 100–200 nm in diameter, which opens encouraging perspectives for the brain biodistribution and clearance of nanoparticulate drug formulations (49). In addition, PEG was shown to directly interact with and repair damaged cellular membranes of neurones after traumatic brain and spinal cord injury (50), which may explain the apparently unusual uptake of our USPIO-PEG nanoparticles by cultured neurones. The same interesting behavior was observed *in vivo*, where these nanoparticles were found in the brain parenchyma after i.v. administration. Their accumulation was much lower than that of USPIO-PHO (i.e. 3 times smaller at 90 min post-injection; 50% of that of USPIO-PHO at 150 min post-injection), but it seems that BBB crossing by these nanoparticles is possible even in the absence of permissive strategies.

To conclude, the results presented in the current work suggest that USPIO-PHO have true potential for labeling amyloid plaques in the brain; it has a nanomolar binding affinity, no toxic effects, and its elimination half-life is about 3 h. Further tests will be made on transgenic mice, aiming to confirm the potential for early AD diagnosis by our vectorized contrast agent.

4. MATERIAL AND METHODS

4.1. Synthesis of USPIO derivatives

The peptides PHO, PHI and P1 were purchased as 8-amino-3,6-dioxaoctanoyl derivatives (PolyPeptide, Strasbourg, France). They were conjugated to the carboxyl groups exposed by the coating of USPIO through their amino-terminal groups as
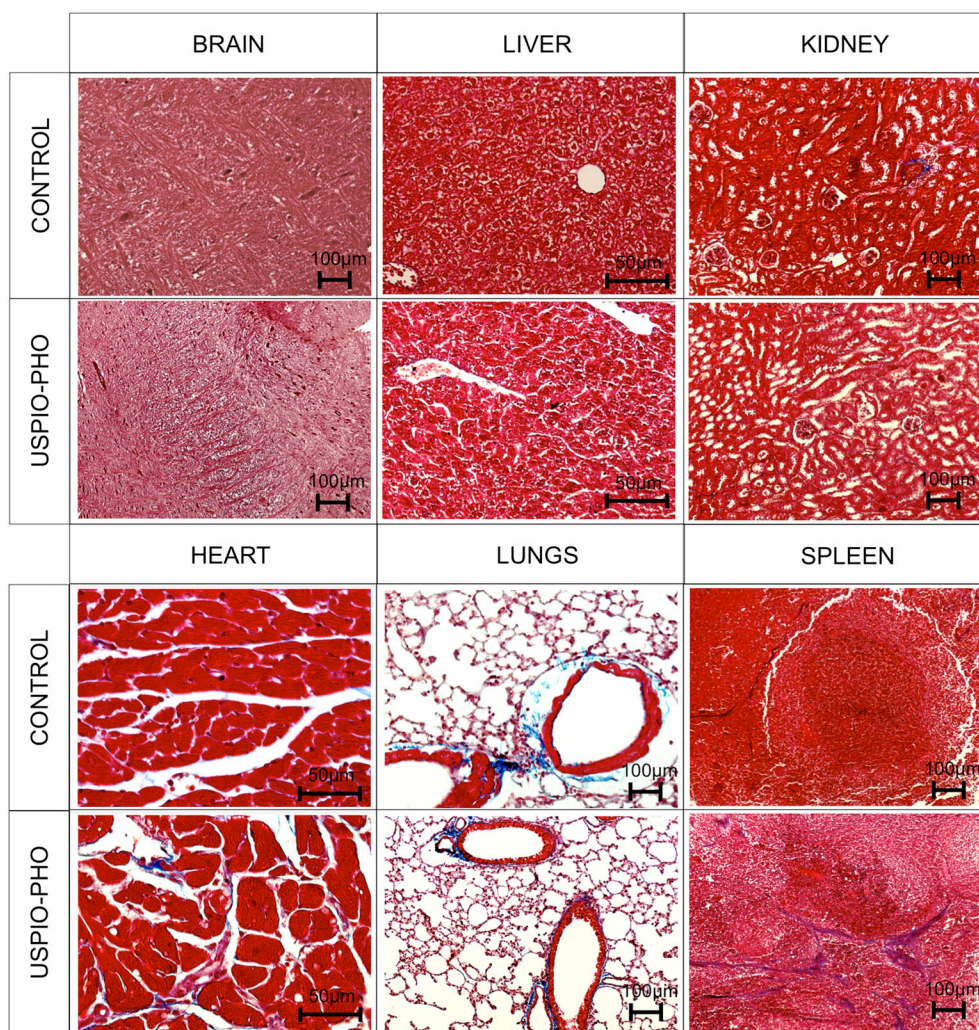
Figure 6. Masson's Trichrome coloration in brain, liver, kidney, heart, lungs and spleen of NMRI mice one week after USPIO-PHO administration, compared with controls (uninjected mice).

previously described (29,51). The vectorized nanparticles were rendered stealth by a PEG coat [O-(2-aminoethyl)-O-methyl-polyethyleneglycol, $M_w \sim 750$ g/mol, Sigma-Aldrich, Bornem, Belgium], which was also used to prepare the nonspecific nano-particles (USPIO-PEG). Some USPIO derivatives were functionalized with putrescine (Sigma-Aldrich) followed by PEG that was coupled to the free carboxyl groups of USPIO.

## 4.2.	Evaluation of the apparent dissociation constants (K_d*) of the vectorized contrast agents for ABP$_{1-42}$ by ELISA

Serial dilutions of the vectorized contrast agents ranging from 5×10^{-2} to 7×10^{-4} M (concentrations are expressed in moles of particles by assuming ~11 000 iron atoms per particle) were incubated (2 h at 37 °C) with ABP$_{1-42}$ immobilized on an ELISA plate. The vectorized contrast agents bound to the target were first detected with 2 µg/ml of a rabbit anti-PEG antibody (Epitomics, Bioconnect, TE Huissen, The Netherlands), which was then identified with 2 µg/ml of an anti-rabbit biotinylated secondary antibody (BA-1000, Vector Laboratories, Brussels, Belgium) diluted in phosphate buffer, followed by using the Vectastain ABC kit (Vector Laboratories). The wells were washed at each step with 0.05% TBS-Tween. The peroxidase staining reaction was performed with

200 µl per well of ABTS [2,2′-azino-bis(3-ethylbenz-thiazoline-6-sulfonic acid), diamonium salt (Sigma-Aldrich), 22 mg in 100 ml of 50 mM sodium citrate, pH 4.0] completed with 0.05% H_2O_2. The OD$_{405}$ was measured and the K_d* values were obtained by fitting the curves of the vectorized contrast agents' concentration expressed on a semi-logarithmic scale (Sigmaplot software).

## 4.3.	Evaluation of *in vitro* cytotoxic effect of the vectorized contrast agents on cellular cultures by MTT assay

The mouse neuroblastoma N18TG2 cell line (kind gift from Mrs Ritu Mishra, Max Planck Institute for Biological Cybernetics, Tuebingen, Germany) was cultured in Dubelcco's modified Eagle medium (DMEM) supplemented with 10% fetal bovine serum (FBS) and 1% penicillin–streptomycin (all from Life Technologies, Gent, Belgium). Differentiation into neurons was induced by reducing the FBS concentration in the culture medium to 0.2%. Human umbilical vein endothelial cells (HUVEC, kind gift from V. Castronovo, ULG, Belgium) were cultured in MCDB131 medium supplemented with 20% FBS, 1% L-glutamine, 0.14% heparin 5000 U/ml and 1% antibiotic-antimycotic (all from Life technologies). Hepatocytes (HepaRG) were cultured with William's E medium supplemented with 13% of HepaRG™ Thaw,
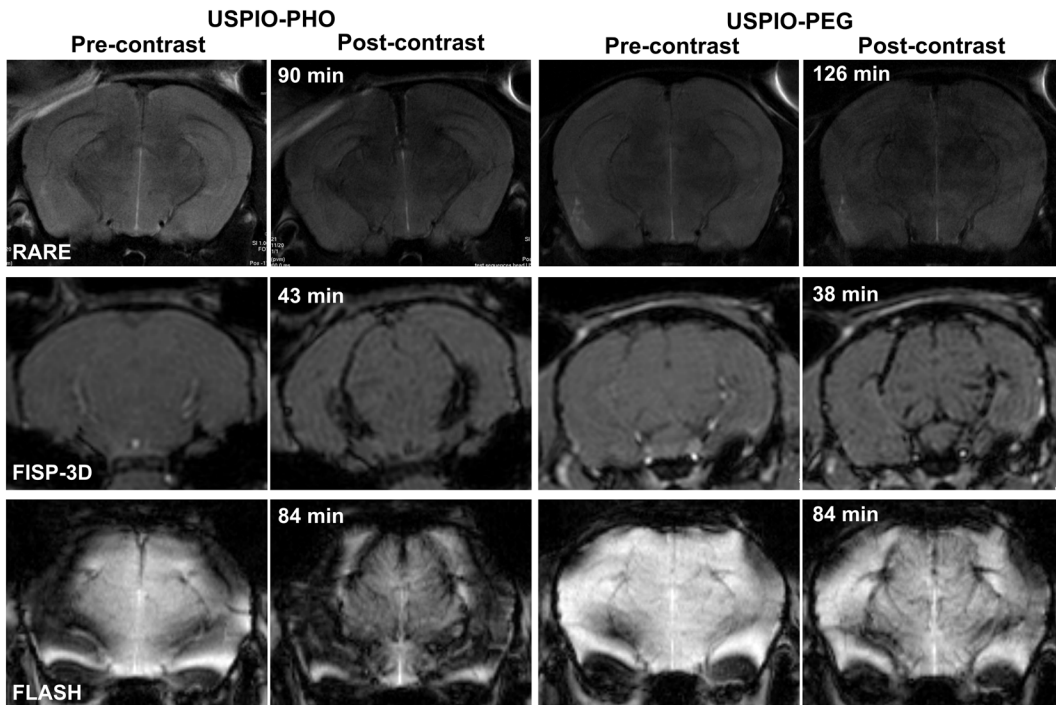
Figure 7. Representative images of the rostral midbrain acquired with various MRI protocols on NMRI mice injected with either USPIO-PHO or USPIO-PEG.
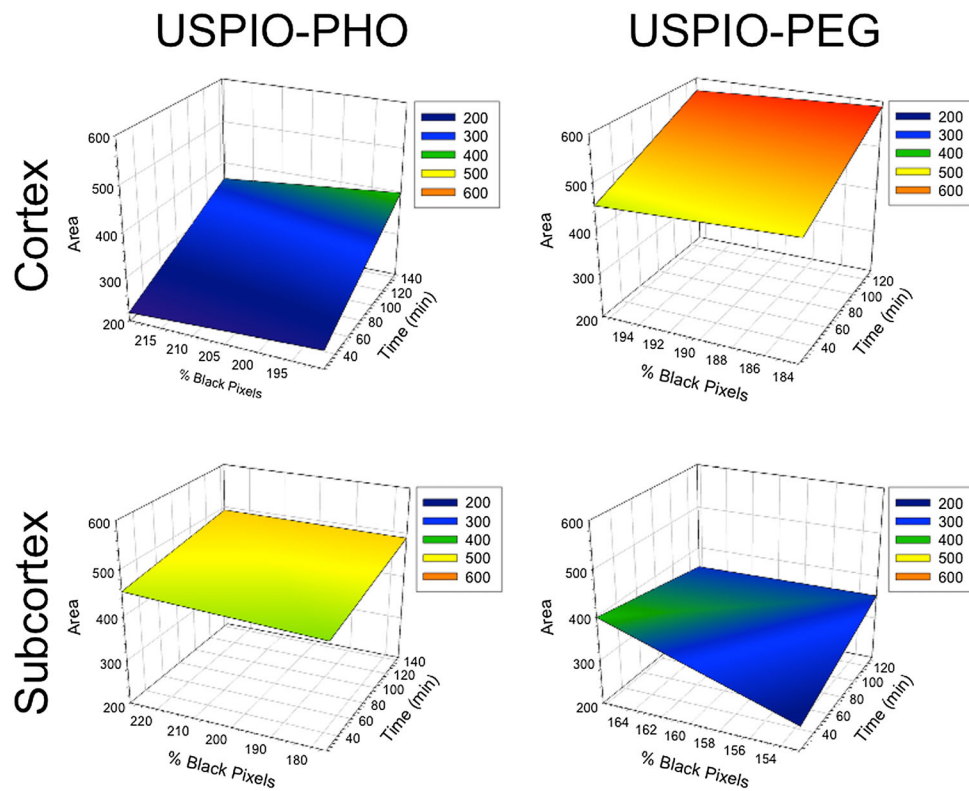

Figure 8. Semi-quantitative analysis of brain MR images obtained with RARE sequence. The relationship between the distribution of black pixels and the contrasted area expressed as a percentage compared with pre-contrast images as a function of time was measured in the cortex (top) and subcortical areas (bottom) and the results were expressed as mesh plots.

Plate, & General Purpose Medium Supplement and 1% GlutaMAX (all from Life Technologies). For toxicity tests, the HepaRG medium was supplemented with 13% HepaRG Tox Medium Supplement (Life Technologies). For the MTT assay (In vitro toxicology assay kit MTT based, Sigma, Bornem, Belgium), the cells were seeded into 96-well plates at a cell density of 2×10^4/well. Cells were then incubated (2 and 24 h, 37 °C) with contrast agents diluted in the culture medium at a concentration
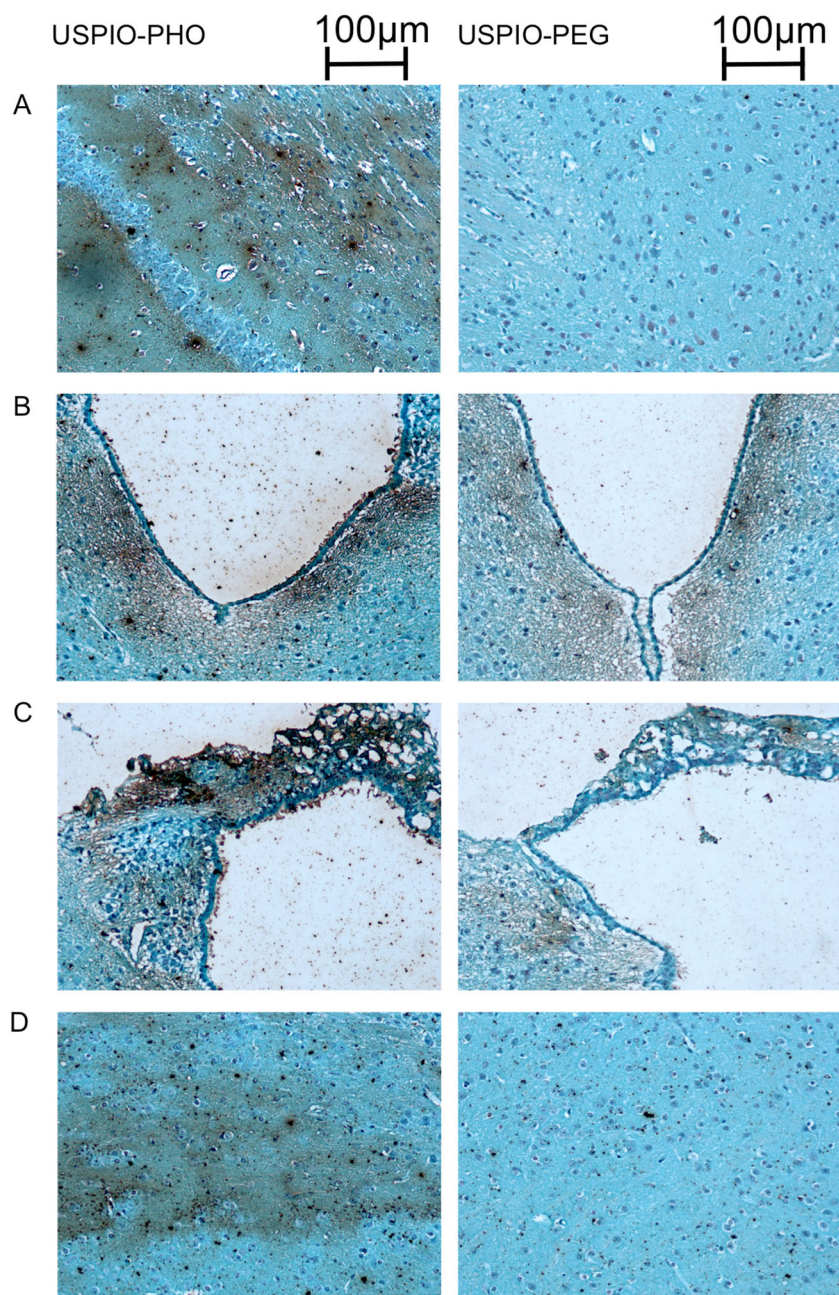
Figure 9. Perls's DAB iron staining of mouse brains 90 min after USPIO-PHO or USPIO-PEG administration. The shown areas correspond to the cortical area above the third ventricle (A), the nervous tissue beneath the dorsal third ventricle (B), the choroid plexus of the dorsal third ventricle (C), and the brain parenchyma beneath the hippocampus (D). The iron is stained in brown.

of 2 mM. This concentration corresponds to the maximum blood concentration at T_0 after the administration of 100 μmol Fe/kg b. w. of contrast agent, as used for the *in vivo* studies described below. The negative control cells were incubated with the culture medium free of contrast agent. The culture medium was then removed and the wells were rinsed with 300 μl/well of PBS. The cells were subsequently incubated (3 h, 37 °C) with MTT solution diluted 1:10 in the culture medium. The resulting formazan crystals were dissolved by adding 100 μl/well DMSO. The absorbance was then measured at 570 nm, with background absorbance at 690 nm subtracted. The percentage of viability was calculated as the ratio of viable treated cells over viable negative control cells (untreated cells).

4.4. Evaluation of internalization of vectorized contrast agents by cells via fluorescent labeling of cellular lysosomes

The test was carried out in triplicate on neurons obtained by differentiation of the neuroblastoma N18G2 cell line by serum privation, as well as on HUVEC. They were incubated (2 h, 37 °C) with contrast agents diluted in the culture medium at a concentration of 2 mM. The reagents used for this experiment were Hoechst 33342 and Lysotracker® Red DND-99 (Image-mITT LIVE lysosomal and nuclear labeling kit, Life technologies), marking cell nuclei in blue (461 nm emission) and lysosomes in red (590 nm emission) to allow their quantification on microphotographs by ImageJ software (National Institutes of Health, USA).

Table 5. Transverse relaxivity, r_2, of each vectorized contrast agent measured at 60 MHz and 37 °C in blood plasma, urine and distilled water. The results are expressed as means ± SEM

r_2 (s^{-1} mM^{-1})	USPIO-PHO	USPIO-PHI	USPIO-P1	USPIO-PEG
Plasma	108.78 ± 11.83	118.73 ± 6.99	111.03 ± 6.32	107.75 ± 4.85
Urine	90.55 ± 0.10	98.17 ± 0.06	100.79 ± 0.13	128.05 ± 2.33
Distilled water	80.19 ± 1.22	97.35 ± 0.70	117.36 ± 0.11	87.04 ± 1.13

The relative fluorescent labeling (RFL) was calculated using the equation shown below, using the signal intensity (SI) values measured on three to six different microscopic fields:

$$RFL = \left(\frac{SI_{sample}}{Number\ of\ cells}\right) / \left(\frac{SI_{negative\ controls}}{Number\ of\ cells}\right) \times 100$$

4.5. Evaluation of internalization of USPIO-PHO by cells via measurement of iron concentration

Neurons obtained by differentiation of the neuroblastoma N18G2 cell line and HUVEC were incubated (2 h, 37 °C) with USPIO-PHO or USPIO-PEG diluted in the culture medium at a concentration of 2 mM. Control cells were incubated in culture medium alone. Subsequently, the cells were rinsed three times with PBS and the solution was removed by centrifugation at 4500 rpm for 10 min. After mineralization (100 μL of 5 M HCl for 2×10^6 cells, 3 h at 80 °C, bain marie), the iron concentration in cell samples was determined by relaxometry on a Bruker Minispec Mq60 working at 60 MHz (Bruker, Karlsruhe, Germany) based on a calibration curve.

4.6. Evaluation of the biodistribution of vectorized contrast agents in plasma and organs by NMR relaxometry

The experiments fulfil the requirements of the Ethical Committee of our institution. NMRI mice (average weight 32 g; Harlan, Horst, The Netherlands) were anesthetized with 50 mg/kg b.w., i.p., of Nembutal, and were injected with 100 μmol Fe/kg b.w. of each of the seven contrast agents (USPIO-PHO, USPIO-PHI, USPIO-P1, USPIO-PEG, USPIO-PHO-put, USPIO-PHI-put, USPIO-put; $n = 3$/experimental group). The control animals were left untreated. The mice were sacrificed with a lethal dose of Nembutal and the blood, urine and organs (brain, liver, kidneys, spleen and lungs) were collected at various time intervals (1, 2, 5, 15, 30, 90 and 150 min, 4, 12 and 24 h, 1 week, and 1, 3 and 6 months) after the injection of each contrast agent for subsequent analysis. The blood was collected on heparin for plasma isolation. The organs were rinsed with 15 ml of PBS by transcardial perfusion, and they were sampled for subsequent histology study and measurement of the transverse relaxation time of the water protons (T_2) by using a Bruker Minispec mq60 working at 60 MHz and 37 °C. The transverse relaxation rate ($R_2 = 1/T_2$) was calculated for each organ, and the concentration of USPIO derivatives in blood plasma and urine was calculated by relating the R_2^{Norm} (normalized by subtracting the R_2 of control animals) of test samples to the transverse relaxivity, r_2, of each vectorized contrast agent as measured in blood plasma and urine (Table 5). A two-compartment distribution model was used to calculate the pharmacokinetic parameters such as the elimination half-life ($T_{e1/2}$), the volume of distribution steady state (VD_{ss}) and the total clearance (Cl_{tot}) [51–53].

4.7. Evaluation of *in vivo* toxicity by measurement of ALT concentration in plasma samples

ALT was measured on the plasma samples collected during biodistribution studies with an ALT assay kit (Abcam, Cambridge, UK) according to the manufacturer's recommendations. Briefly, a standard curve is performed with the pyruvate standard solution diluted to obtain a concentration range of 0.1–0.5 nmol/μl. Plasma samples were diluted to 1:4 in the reaction buffer, and 100 μl of the reaction mix provided in the kit was added to 20 μl of both standard solutions and test samples. The absorbance was measured at 570 nm before and after incubation of the different solutions at 37 °C for 40 min. The change in absorbance is generated by the pyruvate oxidation.

4.8. Evaluation of *in vivo* toxicity by measuring creatinine concentration in urine samples

Creatinine concentration was evaluated in urine samples collected during previous manipulations on NMRI mice with a creatinine assay kit (Abcam). A standard curve was obtained with a creatinine standard solution diluted with buffer at a concentration ranging from 0.04 to 0.2 nmol/μl. Urine samples were diluted 1:10 in the reaction buffer and 50 μl of the reaction mix provided in the kit was added to 50 μl of both standard solutions and test samples. After incubating at 37 °C for 1 h, the optical density was measured at 570 nm and the creatinine concentration of the test samples was determined as a function of the standard curve.

4.9. Evaluation of the tissue integrity of the sampled organs by Masson's Trichrome staining

The sampled organs were fixed in a 4% solution of paraformaldehyde, then dehydrated and paraffin embedded before cutting 5 μm thick sections, dewaxing and rehydration. The Accustain® kit (Sigma-Aldrich) was used to perform the Masson's trichrome stain, which was carried out according to the manufacturer's standard procedure. Briefly, the histological sections are first treated with Bouin's solution to intensify the final coloration. The nuclei are then stained with Weigert's iron hematoxylin, while cytoplasm and muscle are finally stained with Biebrich scarlet-acid fuchsine. The collagen is stained with aniline blue subsequent to the treatment with phosphotungstic and phosphomolybdic acid. The tissue sections are then rinsed in acetic acid and distilled water and finally mounted in a permanent medium after dehydration.

4.10. *In vivo* evaluation of the ability of USPIO-PHO to cross the BBB by MRI studies

To determine which MRI sequences are the most efficient to study the effect of our vectorized contrast agent, several protocols were tested on NMRI mice to allow further studies on APP/PS1 DE9 transgenic mice. Images were acquired at the level of the head on a 300 MHz (7 T) Bruker Biospec imaging system (Bruker, Ettlingen, Germany) equipped with a Pharmascan horizontal magnet and a circular polarized MRI transceiver coil (55 mm x 23 mm; frequency of 3 MHz; maximum RF of 5 ms), using four different imaging protocols: Rapid Acquisition with Relaxation enhancement (RARE) (time of repetition (*TR*)/time of echo (TE) = 3000/30 ms, RARE factor = 4, number of experiments (NEX) = 4, field of view (FOV) = 2.5 cm, matrix = 512 × 512, slice thickness = 1 mm, 20 axial slices, spatial resolution = 48 μm, time of acquisition (TA) = 25 min 36 s); Fast Imaging with Steady State Precession (FISP)-3D (*TR/TE* = 18/4 ms, NEX = 4, FOV = 2.5 cm, matrix = 256 × 256 × 128, spatial resolution = 98 × 98 × 195 μm, TA = 21 min 19 s); Fast Low Angle Shot (FLASH) (*TR/TE* = 450/15 ms, NEX = 4, FOV = 2.5 cm, matrix = 256 × 256, slice thickness 1 mm, spatial resolution = 98 μm, TA = 5 min 46 s); and Multiple Gradient Echo (MGE)-3D (*TR/TE* = 40/4226 ms, NEX = 2, FOV = 2 × 2 × 2.13 cm, matrix = 222 × 251 × 112, spatial resolution = 90 × 80 × 190 μm, TA = 37 min 29 s). During the MRI studies, the mice were anesthetized with 2% isoflurane (Tem Sega, Lormont, France) delivered by airflow through a nose adapter at 70 ml/min. A small-animal monitoring and gating system was used to monitor animal respiration rate. Mouse body temperature was maintained at 36–37 °C using a warm water circulating system. The contrast agents USPIO-PHO and USPIO-PEG were injected at a dose of 100 μmol Fe/kg b.w.).

Regions of interest were drawn manually on RARE images by using the ImageJ image analysis software in cortical and subcortical areas of the brain, starting with the rostral midbrain and covering 3 mm of the forehead. The percentage of black pixels, as well as the total area and the area fraction in pre-contrast and post-contrast (thresholded to the pre-contrast level) RARE images of the cortical and subcortical areas were estimated using the ImageJ software (51). The same threshold was maintained for all animals. The pixel thresholding is easily assisted by this software, which offers a parametric tool to select a certain range of pixel intensities. The results were expressed as percentage ratio of post-contrast data as compared with the pre-contrast ones.

4.11. Perls'-DAB staining of USPIO derivatives on histological brain samples

The NMRI mice were injected with USPIO-PHO or USPIO-PEG at a dose of 100 μmol Fe/kg b.w. and the brains were sampled 90 min after administration. After transcardial perfusion with PBS, the brains were treated for histological analysis as described above. USPIO derivatives present inside the brain parenchyma were revealed by Perls's DAB iron staining on histological slices (54). For this purpose, they were rehydrated and endogenous peroxidases were blocked 15 min with 1% H_2O_2 in PBS. USPIO derivatives were then detected by staining for 30 min with Perls' working solution (mixing equal volumes of 5% potassium ferrocyanide and 5% HCl). After rinsing three times for 10 min in distilled water, the tissue was treated for 10 min with 0.05% DAB in PBS, pH 7.4, followed by immersion for 10 min in 0.05% DAB supplemented with 0.033% H_2O_2 prepared in PBS, pH 7.4. After rinsing again three times in distilled water, the sections were counterstained with hemalun and Luxol fast blue and mounted in a permanent medium.

4.12. Statistical analysis

Data are presented as means ± standard error of the mean (SEM). The difference between various experimental groups was evaluated by one-way ANOVA, performed with SigmaPlot 11.0 software. For the groups were the equal variance test did not pass, the statistical significance was furthermore confirmed after applying the Holm–Sidak and Bonferroni tests. Results were considered statistically significant at $p < 0.05$.

REFERENCES

1. Sarazin M, Dubois B. Mild cognitive impairment or pre-demential Alzheimer's disease? Rev Neurol (Paris) 2002; 158(10 Suppl): S30–S34.
2. Soffer D. Cerebral amyloid angiopathy – a disease or age-related condition. Isr Med Assoc J 2006; 8(11): 803–806.
3. Hardy J, Selkoe DJ. Medicine – the amyloid hypothesis of Alzheimer's disease: progress and problems on the road to therapeutics. Science 2002; 297(5580): 353–356; doi: 10.1126/science.1072994.
4. Medeiros R, Baglietto-Vargas D, LaFerla FM. The role of tau in Alzheimer's disease and related disorders. CNS Neurosci Ther 2011; 17(5): 514–524; doi: 10.1111/j.1755-5949.2010.00177.x.
5. Casetta I, Govoni V, Granieri E. Oxidative stress, antioxidants and neurodegenerative diseases. Curr Pharm Des 2005; 11: 2033–2052; doi: 10.2174/1381612054065729.
6. Li S, Hong S, Shepardson DM, Shankar GM, Selkoe DJ. Soluble oligomers of amyloid β protein facilitate hippocampal long-term depression by disrupting neuronal glutamate uptake. Neuron 2009; 62(6): 788–801; doi: 10.1016/j.neuron.2009.05.012.
7. Wyss-Coray T. Inflammation in Alzheimer disease: driving force, bystander or beneficial response? Nat Med 2006; 12(9): 1005–1015; doi: 10.1038/nm1474.
8. Contestabile A. The history of the cholinergic hypothesis. Behav Brain Res 2011; 221(2): 334–340; doi: 10.1016/j.bbr.2009.12.044.
9. Bozso Z, Penke B, Simon D, Laczkò I, Juhàsz G, Szegedi V, Kasza A, Soòs K, Hetényi A, Wéber E, Tohati H, Csete M, Zarandi M, Fülöp L. Controlled in situ preparation of Aβ(1–42) oligomers from the isopeptide 'iso-Aβ(1-42)', physicochemical and biological characterization. Peptide 2010; 31: 248–256; doi: 10.1016/j.peptides.2009.12.001.
10. Montalto MC, Farrar G, Hehir CT. Fibrillar and oligomeric beta-amyloid as distinct local biomarkers for Alzheimer's disease. Ann NY Acad Sci 2007; 1097: 239–258; doi: 10.1196/annals.1379.023.
11. Larbanoix L, Burtea C, Laurent S, Van Leuven F, Toubeau G, Vander Elst L, Muller RN. Potential amyloid plaque-specific peptides for the diagnosis of Alzheimer's disease. Neurobiol Aging 2010; 31: 1679–1689; doi: 10.1016/j.neurobiolaging.2008.09.021.
12. Walsh DM, Selkoe DJ. A beta oligomers – a decade of discovery. J Neurochem 2007; 101: 1172–1184; doi: 10.1111/j.1471-4159.2006.04426.x.
13. Deane R, Zlokovic BV. Role of the blood–brain barrier in the pathogenesis of Alzheimer's disease. Curr Alzheimer Res 2007; 4: 191–197; doi: 10.2174/156720507780362245.
14. Pascale CL, Miller MC, Chiu C, Boylan M, Caralopoulos IN, Gonzalez L, Johanson CE, Silverberg GD. Amyloid-beta transporter expression at the blood-CSF barrier is age-dependent. Fluids Barriers CNS 2011; 8: 21; doi: 10.1186/2045-8118-8-21.
15. Silverberg GD, Miller MC, Messier AA, Majmudar S, Machan JT, Donahue JE, Stopa EG, Johanson CE. Amyloid deposition and influx transporter expression at the blood-brain barrier increase in normal aging. J Neuropathol Exp Neurol 2010; 69: 98–108; doi: 10.1097/NEN.0b013e3181c8ad2f.

16. Donahue JE, Flaherty SL, Johanson CE, Duncan JA, Silverberg GD, Miller MC, Tavares R, Yang W, Wu Q, Sabo E, Hovanesian V, Stopa EG. RAGE, LRP-1, and amyloid-beta protein in Alzheimer's disease. Acta Neuropathol 2006; 11: 405–415; doi: 10.1007/s00401-006-0115-3.

17. Miller MC, Tavares R, Johanson CE, Hovanesian V, Donahue JE, Gonzalez L, Silverberg GD, Stopa EG. Hippocampal RAGE immunoreactivity in early and advanced Alzheimer's disease. Brain Res 2008; 1230: 273–280; doi: 10.1016/j.brainres.2008.06.124.

18. Jellinger KA, Janetzky B, Attems J, Kienzl E. Biomarkers for early diagnosis of Alzheimer disease: ALZheimer ASsociated gene – a new blood biomarker? J Cell Mol Med 2008; 12(4): 1094–1117; doi: 10.1111/j.1582-4934.2008.00313.x.

19. Freeman SH, Raju S, Hyman BT, Frosch MP, Irizarry MC. Plasma Aβ levels do not reflect brain Aβ levels. J Neuropathol Exp Neurol 2007; 66(4): 264–271; doi: 10.1097/NEN.0b013e31803d3ae4.

20. Burtea C, Laurent S, Port M, Lancelot E, Ballet S, Rousseaux O, Toubeau G, Vander Elst L, Corot C, Muller RN. Magnetic resonance molecular imaging of vascular cell adhesion molecule-1 expression in inflammatory lesions using a peptide-vectorized paramagnetic imaging probe. J Med Chem 2009; 52: 4725–4742; doi: 10.1021/jm9002654.

21. Burtea C, Laurent S, Lancelot E, Ballet S, Murariu O, Rousseau O, Port M, Vander Elst L, Corot C, Muller RN. Peptidic targeting of phosphatidylserine for the MRI detection of apoptosis in atherosclerotic plaques. Mol Pharm 2009; 6: 1903–1919; doi: 10.1021/mp900106m.

22. Hammoud DA, Hoffman JM, Pomper MG. Molecular neuroimaging: from conventional to emerging techniques. Radiology 2007; 245: 21–42; doi: 10.1148/radiol.2451060731.

23. Yang L, Rieves D, Ganley C. Brain amyloid imaging – FDA approval of florbetapir F18 injection. New Engl J Med 2012; 367(10): 885–887; doi: 10.1056/NEJMp1208061.

24. Kung HF, Choi SR, Qu W, Zhang W, Skovronsky D. [18]F stilbenes and styrylpyridines for PET imaging of A beta plaques in Alzheimer's disease: a miniperspective. J Med Chem 2010; 53: 933–941; doi: 10.1021/jm901039z.

25. Sigurdsson EM, Wadghiri YZ, Mosconi L, Blind JA, Knudsen E, Asuni A, Scholtzova H, Tsui WH, Li Y, Sadowski M, Turnbull DH, de Leon MJ, Wisniewski T. A non-toxic ligand for voxel-based MRI analysis of plaques in AD transgenic mice. Neurobiol Aging 2008; 29(6): 836–847; doi: 10.1016/j.neurobiolaging.2006.12.018.

26. Poduslo JF, Curran GL, Peterson JA, McCormick DJ, Fauq AH, Khan MA, Wengenack TM. Design and chemical synthesis of a magnetic resonance contrast agent with enhanced in vitro binding, high blood-brain barrier permeability, and in vivo targeting to Alzheimer's disease amyloid plaques. Biochemistry 2004; 43(20): 6064–6075; doi: 10.1021/bi0359574.

27. Wadghiri YZ, Sigurdsson EM, Sadowski M, Elliott JI, Li Y, Scholtzova H, Tang CY, Aguinaldo G, Pappolla M, Duff K, Wisniewski T, Turnbull DH. Detection of Alzheimer's amyloid in transgenic mice using magnetic resonance microimaging. Magn Reson Med 2003; 50: 293–302; doi: 10.1002/mrm.10529.

28. Dhenain M, El Tannir El TN, Wu TD, Guegan M, Volk A, Quintana C, Delatour B. Characterization of in vivo MRI detectable thalamic amyloid plaques from APP/PS1 mice. Neurobiol Aging 2009; 30(1): 41–53; doi: 10.1016/j.neurobiolaging.2007.05.018.

29. Larbanoix L, Burtea C, Ansciaux E, Laurent S, Mahieu I, Vander Elst L, Muller RN. Design and evaluation of a 6-mer amyloid-beta protein derived phage display library for molecular targeting of amyloid plaques in Alzheimer's disease. Comparison with two cyclic heptapeptides derived from a randomized phage display library. Peptides 2011; 32(6): 1232–1243; doi: 10.1016/j.peptides.2011.04.026.

30. Soenen SJ, De Cuyper M. Assessing cytotoxicity of (iron oxide-based) nanoparticles: an overview of different methods exemplified with cationic magnetoliposomes. Contrast Media Mol Imag 2009; 4(5): 207–219; doi: 10.1002/cmmi.282.

31. Stark WJ. Nanoparticles in biological systems. Angew Chem Int Ed Engl 2011; 50(6): 1242–1258; doi: 10.1002/anie.200906684.

32. Christa Maree Stephan B, Minett T, Pagett E, Siervo M, Brayne C, McKeith IG. Diagnosing mild cognitive impairment (MCI) in clinical trials: a systematic review. BMJ Open 2013; 3(2): doi: 10.1136/bmjopen-2012-001909.

33. Kung HF. The β-amyloid hypothesis in Alzheimer's disease: seeing is believing. ACS Med Chem Lett 2012; 3: 265–267; doi: 10.1021/ml300058m.

34. Cramer PE, Cirrito JR, Wesson DW, Lee CY, Karlo JC, Zinn AE, Casali BT, Restivo JL, Goebel WD, James MJ, Brunden KR, Wilson DA, Landreth GE. ApoE-directed therapeutics rapidly clear β-amyloid and reverse deficits in AD mouse models. Science 2012; 335(6075): 1503–1506; doi: 10.1126/science.1217697.

35. Sanchez PE, Zhu L, Verret L, Vossel KA, Orr AG, Cirrito JR, Devidze N, Ho K, Yu GQ, Palop JJ, Mucke L. Levetiracetam suppresses neuronal network dysfunction and reverses synaptic and cognitive deficits in an Alzheimer's disease model. Proc Natl Acad Sci U S A 2012; 109(42): E2895–E2903; doi: 10.1073/pnas.1121081109.

36. Laurent S, Burtea C, Thirifays C, Rezaee F, Mahmoudi M. Significance of cell 'observer' and protein source in nanobiosciences. J Colloid Interface Sci 2013; 392: 431–445; doi: 10.1016/j.jcis.2012.10.005.

37. Sakono M, Zako T. Amyloid oligomers: formation and toxicity of Abeta oligomers. FEBS J 2010; 277: 1348–1358; doi: 10.1111/j.1742-4658.2010.07568.x.

38. Pagani L, Eckert A. Amyloid-beta interaction with mitochondria. Int J Alzheimers Dis 2011; 2011: 925050; doi: 10.4061/2011/925050.

39. Tortora GJ, Anagnostakos NP. The cardiovascular system: vessels and routes. In Principles of Anatomy and Physiology, 6th edn. Harper & Row: New York, 1990, pp. 605–653.

40. Poduslo JF, Curran GL. Polyamine modification increases the permeability of proteins at the blood-nerve and blood-brain barriers. J Neurochem 1996; 66: 1599–1609.

41. Kandimalla KK, Curran GL, Holasek SS, Gilles EJ, Wengenack TM, Ramirez-Alvarado M, Poduslo JF. Physiological and biophysical factors that influence Alzheimer's disease amyloid plaque targeting of native and putrescine modified human amyloid beta40. J Pharmacol Exp Ther 2006; 318: 17–25.

42. Borlongan CV, Emerich DF. Facilitation of drug entry into the CNS via transient permeation of blood brain barrier: laboratory and preliminary clinical evidence from bradykinin receptor agonist, Cereport. Brain Res Bull 2003; 60: 297–306; doi: 10.1016/S0361-9230(03)00043-1.

43. Deli MA. Potential use of tight junction modulators to reversibly open membranous barriers and improve drug delivery. Biochim Biophys Acta 2009; 1788: 892–910; doi: 10.1016/j.bbamem.2008.09.016.

44. Bartus RT. Translating the therapeutic potential of neurotrophic factors to clinical 'proof of concept': a personal saga achieving a career-long quest. Neurobiol Dis 2012; 48: 153–178; doi: 10.1016/j.nbd.2012.04.004.

45. Rubio-Aliaga I, Daniel H. Mammalian peptide transporters as targets for drug delivery. Trends Pharmacol Sci 2002; 23: 434–440.

46. Demirel Ö, Jan I, Wolters D, Blanz J, Saftig P, Tampé R, Abele R. The lysosomal polypeptide transporter TAPL is stabilized by interaction with LAMP-1 and LAMP-2. J Cell Sci 2012; 125(Pt 18): 4230–4240; doi: 10.1242/jcs.087346.

47. Strazielle N, Ghersi-Egea JF. Physiology of blood-brain interfaces in relation to brain disposition of small compounds and macromolecules. Mol Pharm 2013;10:1473–1491; doi: 10.1021/mp300518e.

48. Masserini M. Nanoparticles for brain drug delivery. ISRN Biochem 2013, article ID 238428; doi: 10.1155/2013/238428.

49. Nance EA, Woodworth GF, Sailor KA, Shih TY, Xu Q, Swaminathan G, Xiang D, Eberhart C, Hanes J. A dense poly(ethylene glycol) coating improves penetration of large polymeric nanoparticles within brain tissue. Sci Transl Med 2012; 4: 149ra119; doi: 10.1126/scitranslmed.3003594.

50. Koob AO, Colby JM, Borgens RB. Behavioral recovery from traumatic brain injury after membrane reconstruction using polyethylene glycol. J Biol Eng 2008; 2: 9; doi: 10.1186/1754-1611-2-9.

51. Burtea C, Ballet S, Laurent S, Rousseaux O, Dencausse A, Gonzalez W, Port M, Corot C, Vander Elst L, Muller RN. Development of a magnetic resonance imaging protocol for the characterization of atherosclerotic plaque by using vascular cell adhesion molecule-1 and apoptosis-targeted ultrasmall superparamagnetic iron oxide derivatives. Arterioscler Thromb Vasc Biol 2012; 32: e36–e48; doi: 10.1161/ATVBAHA.112.245415.

52. Boutry S, Burtea C, Laurent S, Toubeau G, Vander Elst L, Muller RN. Magnetic resonance imaging of inflammation with a specific selectin-targeted contrast agent. Magn Reson Med 2005; 53: 800–807.

53. Burtea C, Laurent S, Colet JM, Vander Elst L, Muller RN. Development of new glucosylated derivatives of gadolinium diethylenetriaminepentaacetic for magnetic resonance angiography. Invest Radiol 2003; 38: 320–333.

54. Moos T, Møllgård K. A sensitive post-DAB enhancement technique for demonstration of iron in the central nervous system. Histochemistry 1993; 99: 471–475.

Supporting information

Additional supporting information may be found in the online version of this article at the publisher's web site.